nanomaterials

MDPI

Article

Conjugation of Functionalized Gold Nanorods and Copper (I)-Based Drug: An Anisotropic Nano Drug Delivery System

Elena Olivieri [1], Simone Amatori [1,2], Chiara Battocchio [1], Giovanna Iucci [1], Martina Marsotto [1,3], Diego Lipani [1], Annarica Calcabrini [4], Marisa Colone [4], Annarita Stringaro [4], Maria Luisa Dupuis [4], Giuseppe Ammirati [5], Alessandra Paladini [5], Francesco Toschi [5], Maura Pellei [6], Carlo Santini [6], Miriam Caviglia [6], Jo' Del Gobbo [6], Luca Tortora [1], Eleonora Marconi [1], Valentin-Adrian Maraloiu [7] and Iole Venditti [1,*]

1 Sciences Department, Roma Tre University, Via della Vasca Navale 79, 00146 Rome, Italy; elena.olivieri@uniroma3.it (E.O.); simone.amatori@ceric-eric.eu (S.A.); chiara.battocchio@uniroma3.it (C.B.); giovanna.iucci@uniroma3.it (G.I.); martina.marsotto@uniroma3.it (M.M.); diego.lipani@unirom3.it (D.L.); luca.tortora@uniroma3.it (L.T.); eleonora.marconi@uniroma3.it (E.M.)
2 CERIC-ERIC, S. S. 14-km 163.5 in AREA Science Park, 34149 Basovizza, Italy
3 Department of Chemical Science and Technologies, Tor Vergata University of Rome, Via della Ricerca Scientifica 1, 00133 Rome, Italy
4 National Center for Drug Research and Evaluation, Istituto Superiore di Sanità, 00161 Rome, Italy; annarica.calcabrini@iss.it (A.C.); marisa.colone@iss.it (M.C.); annarita.stringaro@iss.it (A.S.); marialuisa.dupuis@iss.it (M.L.D.)
5 CNR—Istituto di Struttura della Materia (CNR-ISM), EuroFEL Support Laboratory (EFSL), 00100 Rome, Italy; giuseppe.ammirati@cnr.it (G.A.); alessandra.paladini@cnr.it (A.P.); francesco.toschi@cnr.it (F.T.)
6 School of Science and Technology, University of Camerino, Via Madonna delle Carceri (ChIP), 62032 Camerino, Italy; maura.pellei@unicam.it (M.P.); carlo.santini@unicam.it (C.S.); miriam.caviglia@unicam.it (M.C.); jo.delgobbo@unicam.it (J.D.G.)
7 National Institute of Materials Physics, 405A Atomistilor St., 077125 Bucharest, Romania; maraloiu@infim.ro1
* Correspondence: iole.venditti@uniroma3.it

Abstract

Gold nanorods (AuNRs) were synthesized and optimized with the aim of obtaining strongly hydrophilic nanomaterials, suitable as a drug delivery system (DDS) for copper-based drugs. After careful purification, AuNRs were characterized by ultraviolet–visible–near-infrared spectroscopy (UV–Vis–NIR), showing two typical localized surface plasmon resonance (LSPR) bands in the range 550–750 nm. Fourier Transform Infrared (FT-IR) and high-resolution X-ray photoelectron (HR-XPS) spectroscopies verified the surface functionalization. Transmission electron microscopy (TEM) showed AuNRs with regular shape and size, with an aspect ratio (AR) of 2.6. Dynamic Light Scattering (DLS) measurements confirmed the size and the stability in water for up to 3 months. The AuNRs were conjugated with copper(I) drugs, i.e., $[Cu(PTA)_4]BF_4$ (PTA = 1,3,5-triaza-7-phosphadamantane). The drug loading procedures and efficiency were optimized, and the best loading was η (%) = 50 ± 7%. The non-covalent interactions of the Cu(I) complex with the AuNRs were studied by means of UV–Vis–NIR, ζ-potential, HR-TEM, FT-IR, synchrotron radiation-induced X-ray photoelectron (SR-XPS), and near-edge X-ray absorption fine structure (NEXAFS) spectroscopy measurements. The MTT assay performed on Vero E6 cells showed that AuNRs and AuNR-Cu(I) conjugates had no significant effect on cell viability, being biocompatible, causing a reduction in cell viability only after prolonged exposure.

Keywords: gold nanorods; copper(I)-based drug; drug delivery system; MTT assay; DLS; SR-XPS; NEXAFS

Academic Editor: Jyh-Ping Chen

Received: 4 January 2026
Revised: 27 January 2026
Accepted: 3 February 2026
Published: 6 February 2026

1. Introduction

In the last ten years, nanomaterials have been employed with great success in several areas, including catalysis optics, energy, sensors, and biotechnology [1–7]. In this latter field, gold nanoparticles in particular are enjoying great success, thanks to their simple and versatile synthesis and their high biocompatibility. Among others, gold nanorods (AuNRs) are being studied in biomedical applications, including photothermal therapy, gene/drug transport, and imaging [8–15]. This success is, in part, thanks to the ease with which it is possible to manipulate the AuNR dimensions and aspect ratios (ARs). In addition, their surface can be modified, allowing for conjugation to biomolecules for specific targeting and absorption and/or delivery of drugs [16–19]. To use them for biomedical purposes, it is very important to understand how the different physical and chemical properties of AuNRs have an impact on cells, especially with respect to the presence of surface stabilizers that strongly influence any toxicity and absorption. A particular feature of AuNRs is a double localized surface plasmon resonance (LSPR), one resulting from the excitation of the oscillating electrons transverse to the main axis of the rod and the other from electrons oscillating in the longitudinal direction. The two plasmons have peaks centered around 520 nm and in the near infrared area, from 680 to 1200 nm. By varying the AR, a variation in the position of plasmons is obtained, where the larger the AR becomes, the larger the λ_{max} of the LSPR of the second peak. The advantage of using longer AuNRs for diagnostic–therapeutic purposes depends on the possibility of exciting and tracing them in a simple way through NIR spectroscopy, in which the energy range is close to the "biological window", where the absorption of light radiation by water and hemoglobin, and therefore, by the tissues of the human body, is negligible: this opens up a range of possibilities for the use of AuNRs in the biomedical field [20–24].

The recent literature has shown promising antimicrobial potential for copper(I) and copper(II) complexes, where ligand design, coordination geometry, and metal–ligand interactions also influence biological efficacy [25,26]. These complexes have demonstrated significant antibacterial and antifungal activity, often superior to or equal to standard drugs in biological studies. The integration of nanotechnology-based delivery and delivery systems could improve bioavailability and target specificity, opening new avenues in the treatment of drug-resistant infections.

The immortalized cell line (Vero) established from kidney epithelial cells of the African green monkey (*Chlorocebus sabaeus*) was used in our study for biological tests. The Vero cell line represents one of the most common mammalian immortalized cell lines used as a model in many research applications (high-throughput screenings, 3D cell cultures, drugs/chemicals testing, bioproduction) [27,28]. Moreover, Vero cells, along with their various derivatives, are the most widely used cell culture for the replication of viruses such as SARS-CoV-2, antiviral screening, and virological studies. This is because they offer many advantages: they are easy to maintain, offer high levels of infectivity, and support efficient virus replication and production [29,30]. There are several commercially available Vero cell lines (e.g., Vero, Vero 76, and Vero E6), all derived from the same source. In particular, in our study, the subline E6 (Vero E6) was employed to evaluate the effects of AuNRs and AuNR-Cu(I) conjugates on cell viability to assess their biocompatibility in view of antiviral applications [31].

In this framework, the synthesis of AuNRs was presented with the aim of obtaining strongly hydrophilic anisotropic nanomaterials, suitable for drug delivery and photothermal therapy. AuNRs were synthesized by seed-mediated methods in two steps, and, after careful purification, they were investigated by means of UV–Vis–NIR, FT-IR and synchrotron radiation-induced X-ray photoelectron (SR-XPS) spectroscopies. High-resolution transmission electron microscopy (HR-TEM) observations confirmed nanosizes in a range

useful for our biomedical applications. Moreover, conjugated systems with copper-based drugs, i.e., $[Cu(PTA)_4]BF_4$, were prepared. The drug loading procedures and efficiency (η) were optimized to improve the hydrophilicity and bioavailability of DDS. The best optimized loading is η (%) = 50 ± 10%. The non-covalent interactions of the Cu(I) complex with the AuNR surface were studied using UV–Vis–NIR, FESEM-EDX, FT-IR, SR-XPS and NEXAFS measurements. Moreover, the MTT tests performed with Vero cells allowed us to study their biocompatibility in view of antiviral applications.

2. Materials and Methods

2.1. Materials

Cetyltrimethylammonium bromide ($C_{19}H_{42}BrN$, CTAB, ≥97% Millipore Corporation Merck Italy), tetrachloroauric(III) acid trihydrate ($HAuCl_4 \cdot 3H_2O$, ≥99.9%, Sigma-Aldrich, Italy), sodium borohydride ($NaBH_4$, 99.99%, Sigma-Aldrich), silver nitrate ($AgNO_3$, 99.9%, Carlo Erba, Italy) and L-ascorbic acid ($C_6H_8O_6$, 99%, Sigma-Aldrich) were used as received. Bidistilled water was used in all the procedures. All the other products were reagent-grade chemicals and were used as received by Merck Italy, without further purification. The analytically pure copper(I) complex $[Cu(PTA)_4]BF_4$ (Figure 1) was synthesized by a one-step reaction of $[Cu(CH_3CN)_4]BF_4$ with an excess of PTA in an acetonitrile solution at room temperature. The reaction mixture was stirred overnight and filtered, and the white residue was washed with chloroform and diethyl ether and then dried under vacuum [32,33].

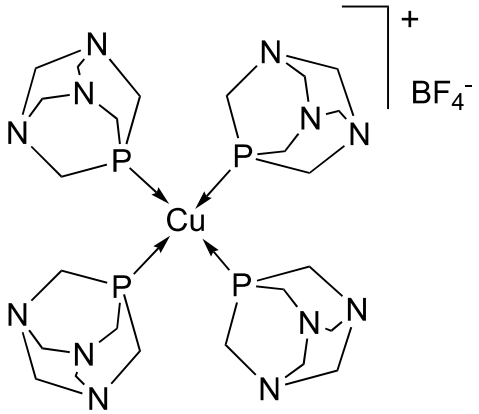

Figure 1. Chemical structure of the copper(I) complex $[Cu(PTA)_4]BF_4$.

2.2. AuNR Synthesis

CTAB-stabilized AuNRs were prepared with a reliable procedure in two steps based on the literature [34,35]. First step: $HAuCl_4$ $3H_2O$ (5 mL, 5×10^{-4} M) and CTAB (5 mL, 0.2 M) water solutions were mixed and degassed by Ar for 5 min. Then, $NaBH_4$ water solution (0.6 mL, 10^{-2} M) was added as a reducing agent to obtain the seed solution in 20 min. Second step: CTAB solution (5 mL, 0.2 M), $HAuCl_4 \cdot 3H_2O$ solution (5 mL, 10^{-3} M), and $AgNO_3$ solution (0.2 mL, 4×10^{-3} M) were mixed (molar ratio Au/CTAB/Ag = 1/200/0.16) under vigorous stirring and with an inert atmosphere (Ar). After 5 min, ascorbic acid solution (0.07 mL, 0.078 M) was added (molar ratio Au/Asc.Ac. = 1/1.092), followed by 0.024 mL of a seed solution. Gradually, the solution turns into a reddish-violet color. The product is left at room temperature (25° C) for 24 h and then purified by centrifugation (13,000 rpm, 15 min, twice washing with deionized water). For more experimental details, see Supporting Information Table S1. Main characterizations: UV–Vis (λ_{max} (nm), H_2O) T-SPR, 515 nm; L-SPR, 740 nm; ζ potential: 46 ± 4 mV; TEM dimensions: transversal side, 20 ± 5 nm, longitudinal side, 60 ± 15 nm.

2.3. AuNR-Cu(I) Conjugate Preparation

$[Cu(PTA)_4]BF_4$ was prepared according to procedures reported in the literature [32,36]. The AuNRs and the Cu(I) complex were mixed in water (Au/Cu = 6/1 *w*/*w*) under gentle stirring (room temperature, 24 h), and then, the suspension was centrifuged (13,000 rpm, 15 min, twice washing with water) to obtain AuNR-Cu(I) as a solid residue. It was stored at T = −18 °C, while the supernatant was used for loading evaluation. Loading efficiencies (η) were calculated by using calibration curves, as in our previous works [37,38]. For each sample, at least 3 independent measurements were carried out, and the mean value and standard deviation were reported. For more experimental details, see Table S2.

2.4. Characterizations

UV–Vis spectra were acquired with a Shimadzu 2401 PC spectrophotometer (200–800 nm), while NIR spectra were obtained with a Nicolet IS50 FT-IR Thermo Scientific, Waltham, MA, USA, spectrophotometer (400–1100 nm) using quartz cells with 1 cm of optical path. FT-IR spectra were acquired in transmittance mode (4000–400 cm^{-1}) with a Bruker Vector 22 using pellets made of the sample and KBr. The ζ potential distribution of AuNRs in H_2O was investigated by means of Zetasizer Ultra Red, Malvern, UK [39–43]. For TEM analysis, images were obtained with a Philips EM 208S instrument (FEI-Thermo Fisher, Waltham, MA, USA, operating at 100 kV, equipped with a Mega-view II SIS Olympus camera; others, with a probe-corrected JEOL JEM ARM200F microscope, Peabody, MA, USA, operated at 200 kV, equipped with a Gatan, UK, Ultrascan CCD camera. Samples were drop-casted on formvar/carbon-supported copper grids, and after a few minutes, the excess liquid was blotted with filter paper, and then the samples were examined.

Synchrotron radiation-induced X-ray photoelectron spectroscopy (SR-XPS) measurements were performed at the SuperESCA beamline at the ELETTRA facility in Trieste (Italy). Photoemission data were collected in fixed analyzer transmission mode (pass energy = 50 eV), with the monochromator entrance and exit slits optimized at 30 and 20 mm, respectively. A photon energy (PE) of 360 eV was used for C1s, P2 and Au4f spectra; for N1s and Ag3d spectral regions, a PE of 520 eV was selected; finally, Cu2p spectra were acquired using a PE of 1100 eV to maximize signal intensities. The total binding energy resolution was about 0.22 eV. As a reference, the energy scale was calibrated using the C1s aliphatic signal at 285.00 eV and the $Au4f_{7/2}$ signal of AuNRs arising from metallic gold atoms, always found at 83.96 Ev [44]. Curve-fitting analysis of the C1s, N1s, P2p, Au4f, Ag3d and Cu2p spectra was performed using Gaussian curves as fitting functions. All spin–orbit doublets were fitted by using the same full width at half-maximum (FWHM) for each pair of components of the same core level. A spin–orbit splitting of 6.0 eV and a branching ratio of $Ag3d_{5/2}/Ag3d_{3/2}$ = 3/2 were selected for Ag3d doublets; a spin–orbit splitting of 3.7 eV and a $Au4f_{7/2}/Au4f_{5/2}$ = 4/3 branching ratio were used for Au4f components; branching ratios of P2p,$Cu2p_{3/2/1/2}$ = 2/1 and spin–orbit splittings of 0.8 eV and 19.8 eV were chosen for, respectively, P2p and Cu2p doublets. When several different species were identified in a spectrum, the same FWHM value was used for all individual photoemission bands. To perform SR-XPS analysis, pristine Cu(I) complex ($[Cu(PTA)_4]BF_4$), AuNRs and conjugates (AuNR-Cu(I)) were deposited onto TiO_2/Si(111) wafer substrates with a drop-casting procedure.

Near-edge X-ray absorption fine structure (NEXAFS) measurements were performed at the BEAR beamline (Bending magnet for Emission Absorption and Reflectivity) at the ELETTRA storage ring, installed at the left exit of the 8.1 bending magnet exit. The apparatus is based on a bending magnet as a source and beamline optics delivering photons from 5 eV up to about 1600 eV with a selectable degree of ellipticity. In these experiments, we used ammeters to measure the drain current from the sample. C and N K-edge spectra

were collected at magic (54.7°) incidence angles of the linearly polarized photon beam with respect to the sample surface. The photon energy and resolution were calibrated and experimentally tested at the K absorption edges of Ar, N2 and Ne. The raw C and N K-edge NEXAFS spectra were normalized to the incident photon flux by dividing the sample spectrum by the spectrum collected on a freshly sputtered gold surface. Spectra were then normalized, subtracting a straight line that fits the part of the spectrum below the edge and assigning the values at 330.00 and 420.00 eV to 1 for C and N, respectively.

2.5. Cell Cultures and Biological Tests

For cell viability assessment, the Vero E6 cell line was employed. This cell line, from the American Type Culture Collection (ATCC), was kindly provided by Dr. Andrea Cara (National Center for Global Health, Istituto Superiore di Sanità, Rome, Italy). Vero cells are normal kidney epithelial cells isolated in 1962 from an African green monkey (*Chlorocebus sabaeus*). They did not originate from a tumor, but they became a continuous/immortalized cell line through spontaneous mutations during culture. Vero cells are characterized by an aneuploid karyotype (abnormal chromosome number), typical of immortalized lines. Cells were grown in DMEM (Dulbecco's Modified Eagle's Medium, Euroclone, Thermo Fisher Scientific, Waltham, MA, USA) supplemented with 10% fetal bovine serum (FBS) (Corning, Charlotte, NC, USA), 1% penicillin (50 U-mL)–streptomycin (Gibco), 1% non-essential amino acids (Euroclone), 1% Sodium Pyruvate (Gibco) at 37 °C, and in an atmosphere containing 5% CO_2 and sub-cultivated at confluence. To evaluate the effects of AuNRs and AuNR-Cu(I) conjugate treatments on Vero E6 cell viability, the MTT assay was performed. Cells were seeded into a 96-well plate (Nunclon, Thermo Fisher Scientific, Waltham, MA, USA) at a density of 1.8×10^4 cells/well. After 24 h, cells were exposed to different concentrations of AuNRs and AuNR-Cu(I) conjugates (0.025, 0.05, 0.25, 0.5 and 1 μg/mL) in cell culture medium for 24, 48 and 72 h. Then, the medium was removed. and 100 μL of MTT (3-(4,5-dimethylthiazol-2-yl)-2,5-diphenyltetrazolium bromide) solution (Sigma-Aldrich, USA) (0.5 mg/mL) was added to each well for 2 h. At the end of this period, cells were dissolved by adding 100 μL/well of DMSO (Merck, Germany). Absorbance was read at 570 nm by a microplate reader (Varioskan™ LUX multimode, Thermo Fisher Scientific, Waltham, MA, USA). Data were expressed as a relative % of cell viability, calculated as the ratio of the absorbance value of the treated cells to the absorbance value of the control cells [$(\text{absorbance}_{\text{treated}}/\text{absorbance}_{\text{control}}) \times 100$]. All experiments were performed in triplicate in at least three independent experiments.

2.6. Statistical Analysis

In cell viability experiments, the results are expressed as mean ± SD. Statistical data analysis was performed using the GraphPad PRISM 10 software (unpaired *t*-test). Statistical significance was assessed by the one-way ANOVA test, followed by the Bonferroni test or the Tukey test. The differences in the means are considered statistically significant with p-values ≤ 0.05.

3. Results and Discussion

3.1. AuNR Synthesis

As is well known, in AuNR synthesis, the size and aspect ratio of the particles can be modulated by varying the experimental parameters, such as the temperature, time, capping agent, reducing agent, and molar ratios of the various reagents used [34,35]. Moreover, suitable surface functionalization can achieve high hydrophilicity, which is the main aim for drug delivery applications. In such cases, AuNRs can act as a vehicle to achieve a targeted and controlled release of the drug, in many cases also improving bioavailability [45–48]. The

synthesis proposed here to obtain strongly hydrophilic AuNRs is based on the use of a seed and involves two steps, both in the aqueous phase. In the first step, the seed is produced starting with Au^{3+} ions, using a strong reducing agent, such as sodium boron hydride, and a capping agent, such as CTAB. In this step, small-sized particles are produced, which will be used in the second step. Specifically, in the following step, always in the presence of CATAB and Au^{3+} ions, a milder reducing agent, ascorbic acid, silver ions, and the seed were added to the mix. These conditions promote the growth of anisotropic particles, with peculiar optical properties, such as two surface plasmon resonance peaks (two LSPR bands) related to the length/thickness ratio or aspect ratio (AR): the transverse and longitudinal bands (T-LSPR and L-LSPR). AuNRs are more easily polarized longitudinally, meaning that LSPR occurs at a lower energy and, thus, a higher wavelength. As the aspect ratio (ratio of length to width) of a nanorod is increased for a fixed diameter, the L-LSPR and T-LSPR are both affected; however, the longitudinal axis is more polarizable and more sensitive to aspect ratio changes. In AuNRs, the L-LSPR wavelength can be tuned from 550 nm to over 2000 nm by adjusting to longer aspect ratios, while the T-LSPR remains relatively constant at ~510–520 nm. It is reported in the literature that AuNRs can show a shift of a few nanometers in the T-LSPR absorption band (505–520 nm), induced by an increase in the aspect ratio from 1.7 to 5.2 [49,50]. On the other hand, the L-LSPR can move from 590 to 935 nm when the aspect ratio increases from 1.7 to 5.2. The critical experimental parameters to control the aspect ratio are mainly in the second step and are the amount of reducing agent (i.e., ascorbic acid), the amount of $AgNO_3$, and the volume of the seed solution used. Regarding ascorbic acid (AA), it is possible to note an increase in the length of the nanorods when the concentration of the reducing agent decreases. In fact, by using a greater quantity of AA, the speed at which Au^{3+} is reduced is faster, and the growth rate of the AuNRs is faster; therefore, shorter AuNRs are formed. Figure 2 shows two different sizes of AuNRs obtained by using different AA volumes (0.078 M) during the second step of the synthesis: for AuNRs-1, the AA volume = 140 µL, and for AuNRs-2, the AA volume = 175 µL. As expected, the dimensions increase by decreasing the reducing agent amount, i.e., AA, the distance between the transverse and longitudinal plasmon peaks increases from 168 to 260 nm, and the AR increases from 2.5 for AuNR-1 to 3.8 for AuNRs-2.

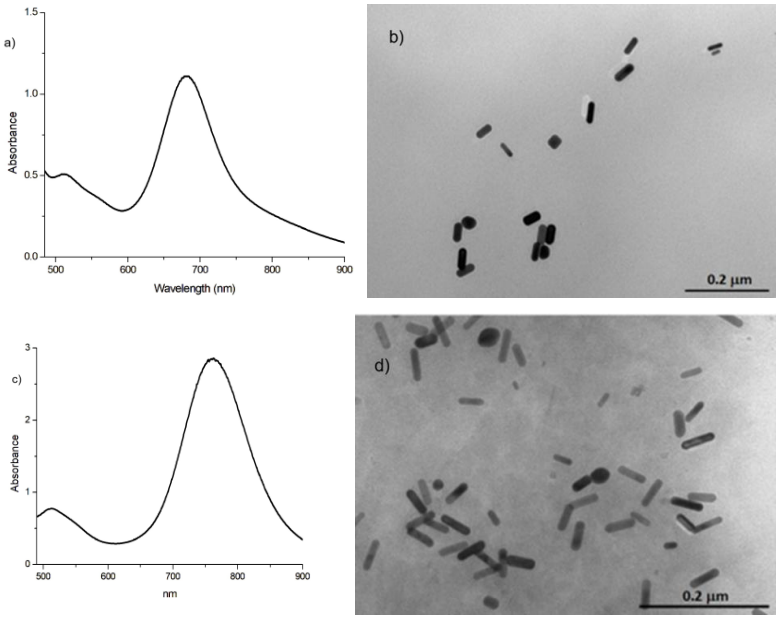

Figure 2. (**a**) NIR of AuNRs-1 with λ_{max} 515 nm and 683 nm; (**b**) TEM image of AuNRs-1 with A.R. = 2.5; (**c**) NIR of AuNRs-2 with λ_{max} 518 nm and 778 nm; (**d**) TEM image of AuNRs-2 with A.R. = 3.8.

The main parameter that must be modulated in order to obtain nanorods of a desired size is the amount of $AgNO_3$. The role of $AgNO_3$ is linked to the anisotropic growth of the rods since, as explained in the literature, the silver is incorporated into the mass of the nanorods by binding the Br of the CTAB. To study the effect of this parameter, different concentrations of $AgNO_3$ were used, and it was observed that as the concentrations increased, two plasmons at distant wavelengths were highlighted, as also reported in the literature. However, the addition of $AgNO_3$ above a certain threshold limits the growth of the rod [51,52]. The volume of seed solution used also influenced the growth of the AuNRs, in a proportional way: smaller nanorods correspond to lower concentrations of seed solution. Figure 3 shows this typical trend of the UV–Vis–NIR spectra as the quantities of $AgNO_3$ and seed solution vary, which also confirms the proposed synthetic protocol that was expected from the literature [53,54].

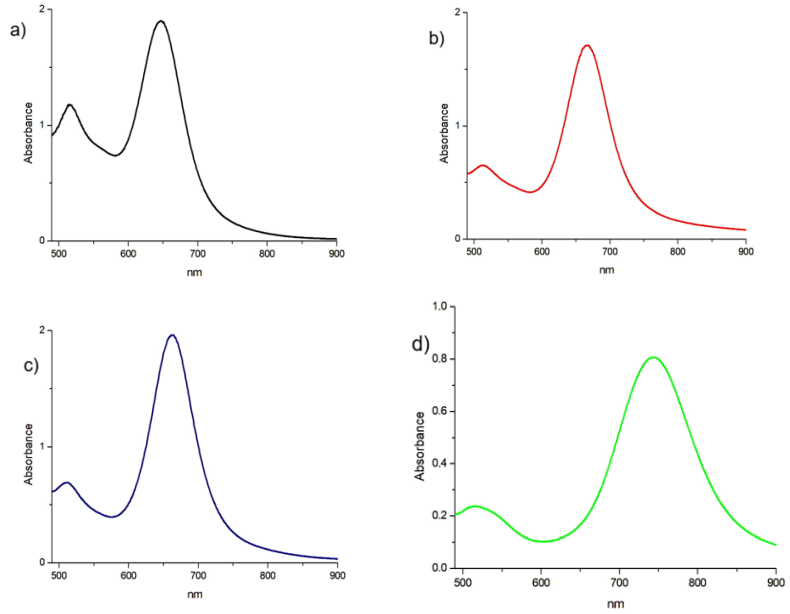

Figure 3. Vis–NIR spectra of AuNRs using different experimental conditions in the second step: (**a**) AuNRs with λ_{max} 520 and 654 nm using [$AgNO_3$] = 0.002 M; (**b**) AuNRs with λ_{max} 520 and 670 nm using [$AgNO_3$] = 0.008 M; (**c**) AuNRs with λ_{max} 516 and 662 nm using volume of seed solution = 12 µL; (**d**) AuNRs with λ_{max} 518 and 744 nm using volume of seed solution = 24 µL.

3.2. Cu(I)-Complex Loading on AuNRs

The synthesized AuNRs were found to be highly hydrophilic and stable in an aqueous environment, as confirmed by UV–Vis and ζ potential measurements performed immediately after synthesis and after 3 months (see Supporting Information, Figure S1). These AuNRs are particularly suitable for drug delivery, and in this study, the aim is to conjugate them with the Cu(I) complex $[Cu(PTA)_4]BF_4$ to increase the final bioavailability. The loading protocol was based on the simple physical contact of AuNRs and Cu(I) complexes that can be physically adsorbed [37,46]. On the basis of these considerations, the loading protocol for AuNRs and the Cu(I) complexes was performed in a water solution at room temperature (25 °C) under gentle stirring. In Figure 4a, the value of the loading efficiency, η (%), was reported for different Cu(I)/Au *w*/*w* ratios: the best result was obtained from the ratio Cu(I)/Au = 1/6, reaching an η (%) of 50 ± 7%. The conjugate is prepared with a gold/copper *w*/*w* ratio of Au/Cu(I) = 6/1, and since the loading efficiency is 50%, the conjugate will have a *w*/*w* ratio of Au/Cu(I) = 12/1. Therefore, for every mg of AuNR-Cu(I) conjugate, about 0.08 mg is copper. The colloidal stability was confirmed by Z potential measurements after 9 months (data reported in SM-Figure S1b).

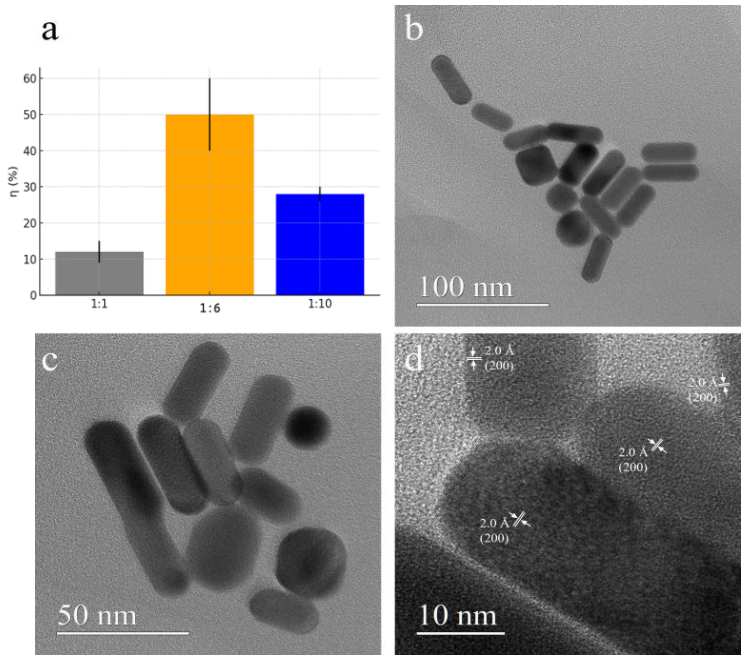

Figure 4. Conjugated system: (**a**) loading percentage of Cu(I) complex on AuNRs by putting different amounts (weight/weight ratio) in contact for 24 h: in gray, a 1:1 ratio with η (%) = 12 ± 3%; in orange, 1:6 with η (%) = 50 ± 7%; and in blue, 1:10 with η (%) = 28 ± 2%; (**b**,**c**) CTEM images show that the predominant morphology is nanorods; (**d**) HRTEM image of well-crystallized AuNRs.

Morpho-structural investigations were performed on the conjugate with the highest loading, and some conventional TEM (CTEM) images are reported in Figure 4b–d, showing regular shape particles and low aggregation phenomena. These images show nanorods with a diameter ranging from 14 to 19 nm and a length from 32 nm to 43 nm. A high-resolution TEM (HRTEM) image (Figure 4d) demonstrates that nanoparticles are well crystallized. In the image, 2.0 Å lattice fringes corresponding to (200) planes of Au crystallized in the cubic structure are easily observed.

3.3. XPS Characterization

Synchrotron radiation-induced X-ray photoelectron spectroscopy (SR-XPS) measurements were carried out on the pristine AuNRs, on the $[Cu(PTA)_4]BF_4$ coordination compound, and on the AuNRs/$[Cu(PTA)_4]BF_4$ (namely, AuNR-Cu(I)) complex system deposited onto TiO_2/Si(111) wafer surfaces by following a drop-casting procedure. Data collected on $[Cu(PTA)_4]BF_4$ were already published and will be briefly summarized here, and they will be used as a reference for the analysis of the more complicated AuNR-Cu(I) adduct [34]. All SR-XPS data were analyzed by following a peak-fitting procedure, allowing us to identify the components arising from the chemical elements with different atomic environments; all peak-position BEs (binding energies), FWHM values, atomic ratios (relative intensities), and assignments are reported in Supporting Information Table S3. For AuNRs, C1s, N1s, Ag3d and Au4f core-level signals were collected and analyzed. The C1s spectrum is reported in Figure 5a. The spectrum appears to be a composite, and at least four spectral components can be individuated by following a peak-fitting procedure: the peak at the lowest BE (285.0 eV) is due to aliphatic C–C groups of ascorbate and impurities, always found on samples prepared in air; the peaks at about 286.4 and 287.8 eV are attributed to C–N and C–OH functional groups of ascorbate; the contribution at 289.2 eV is attributed to COOH impurities on the sample surface. The N1s spectrum (Figure 5b) is made of two components: the first at the lowest BE is associated with C–N nitrogens; the other, at around 400.0 eV, is associated with protonated nitrogen of CTAB. The Ag3d

spectrum (Figure 5c) shows two pairs of spin–orbit ($Ag3d_{5/2}$, $Ag3d_{3/2}$) doublets, of which we consider the $Ag3d_{5/2}$ component as the reference. The $Ag3d_{5/2}$ signal at 367.3 eV is due to metallic bulk Ag(0) atoms, while those around 368.1 eV are due to substrate interface Ag atoms of the nanorods. The Au4f spectrum (Figure 5d) shows two pairs of spin–orbit ($Au4f_{7/2}$ and $Au4f_{5/2}$) doublets, of which we consider the $Au4f_{7/2}$ component as the reference. The $Au4f_{7/2}$ signal around 83.9 eV is due to metallic bulk Au(0) atoms of NRs, while the one at 84.5 eV arises from surface NR Au atoms.

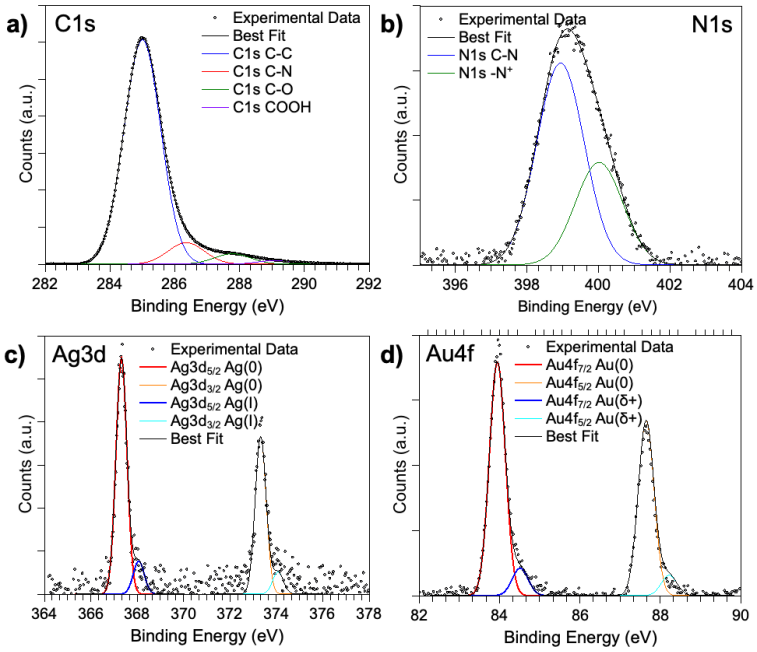

Figure 5. SR-XPS spectra collected at (**a**) C1s, (**b**) N1s, (**c**) Ag3d and (**d**) Au4f core levels on the pristine AuNRs.

SR-XPS data collected on AuNR-Cu(I) were analyzed and compared with $[Cu(PTA)_4]BF_4$ (namely, the Cu(I) complex) and with the data collected on AuNRs and discussed above. The C1s spectrum of AuNR-Cu(I) (Figure 6a, top) shows all the components already observed in the pristine AuNR and Cu(I) complex, as expected: the C-C signal is at 285.0 eV BE, C-N is superimposed with a C-P contribution at about 286 eV BE, C-O is at 287 eV, C=O is around 288 eV BE, and a very low peak arising from COOH groups at a high BE (289 eV). It is noteworthy that the last three contributions in Cu(I) arise from adventitious carbon impurities, as already observed in other works [33]. As for N1s and P2p signals (Figure 6b,c), they both indicate the successful functionalization of AuNRs with a Cu(I) complex. In fact, the N1s spectrum of AuNR-Cu(I) contains the two main features expected for the pristine Cu(I) coordination compound, as well as a third component at high BE values (401 eV) due to the positively charged quaternary amine of CTAB, while the P2p spectra observed in $[Cu(PTA)_4]BF_4$ and AuNR-Cu(I) are analogous, also confirming the chemical stability of the Cu(I) complex upon interaction with the AuNR surface. Finally, the $Cu2p_{3/2}$ spectra collected at high resolution on the pristine Cu(I) complex and AuNR-Cu(I) show that the copper ion is partially oxidized from Cu(I) to Cu(II) in the nanosystem (Figure 6d). However, this is an expected behavior since the conjugation procedure is carried out in an aqueous environment; indeed, this finding was already observed and discussed in a recent publication [33]. Furthermore, the prolonged exposure to the X-ray beams necessary to acquire good data on the very diluted AuNP-Cu(I) sample could induce copper oxidation at the surface; this is highly visible in the XPS spectrum since this is a surface-sensitive technique with a sampling depth of 3–5 nm [53].

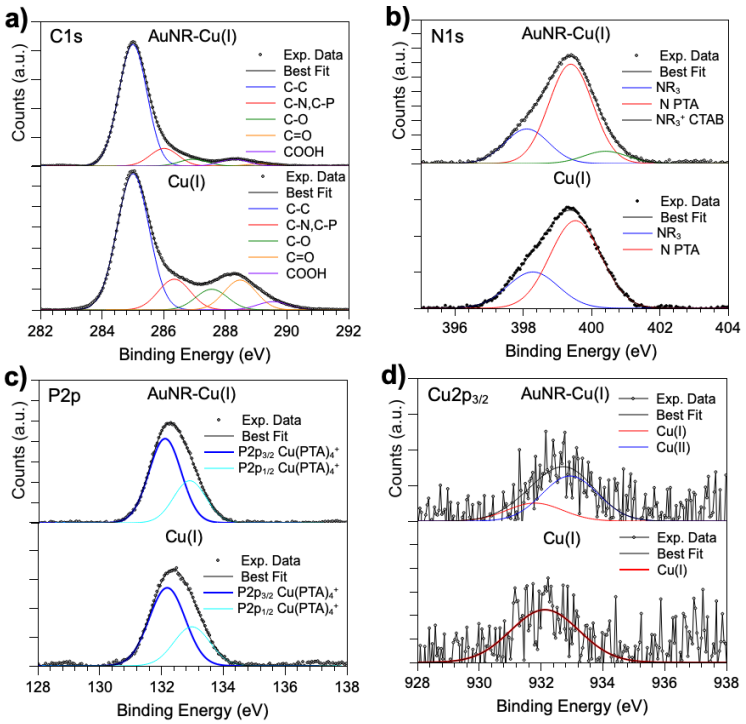

Figure 6. High-resolution SR-XPS spectra peak fit results for AuNR-Cu(I), compared with the same core level region measured on a pristine Cu(I) complex: (**a**) C1s; (**b**) N1s; (**c**) P2p; (**d**) Cu2p3/2.

3.4. NEXAFS Characterization

NEXAFS spectroscopy measurements were carried out at the C and N K-edges on all samples in a solid state, prepared as samples for SR-XPS. The NEXAFS C K-edge spectrum of AuNR is reported in Figure 7a. The feature at about 288.7 eV is associated with the C 1s $\rightarrow$ π^* transition of the C=O molecular orbital due to residual ascorbic acid molecules adsorbed on the nanorods surface; a shoulder at about 288 eV with a σ^* resonance caused by the C−H groups and Rydberg features; and additional features around 293 and 303 eV, which can be assigned to 1s $\rightarrow$ σ^* transitions by C−C and C=O molecular groups, respectively [54,55]. The peak at 288.7 eV also appears in the spectrum of $[Cu(PTA)_4]BF_4$ (Figure 7b), while the σ^* resonance at 293 eV appears to be much more intense due to contributions from the many C-C bonds of the PTA ligand. The C K edge spectrum of the AuNR-Cu(I) sample (Figure 7c) appears as a combination of the spectra of $[Cu(PTA)_4]BF_4$ and AuNRs. The N K-edge spectrum of AuNR (reported in Figure 7d) shows a sharp peak at 402 eV, assigned to the N 1s $\rightarrow$ σ^* transition of the positively charged nitrogen of CTAB. In the spectrum of $[Cu(PTA)_4]BF_4$ (Figure 7e), this peak appears to be more intense, with a shoulder at about 405 eV; pre-edge transitions, possibly due to Rydberg features, are also evident below the edge. Again, the C K spectrum of the AuNR-Cu(I) sample (Figure 7f) is a combination of the spectra of $[Cu(PTA)_4]BF_4$ and AuNRs.

3.5. FTIR Characterization

The FTIR spectra of the $[Cu(PTA)_4]BF_4$ complex and of the AuNR-Cu(I) conjugate in the spectral regions where the most diagnostic peaks are located are shown in Figure 8. The high wavenumber region (4000–2700 cm^{-1}) of the spectrum of $[Cu(PTA)_4]BF_4$ (Figure 8a) shows peaks related to the stretching vibrations of C-H ($\nu_{C\text{-}H}$ 2890 cm^{-1}) and O-H ($\nu_{O\text{-}H}$ at about 3500–3600 cm^{-1}); the latter is due to physisorbed water. The bending vibrations of the corresponding bonds are found at 1470 and 1330 cm^{-1} ($\delta_{C\text{-}H}$) and at 1560 cm^{-1} ($\delta_{O\text{-}H}$). The C-N stretching vibration due to the PTA ligand ($\nu_{C\text{-}N}$) is located at 1200 cm^{-1}, while the peak at 1070 cm^{-1} ($\nu_{B\text{-}F}$) can be assigned to the BF_4 anion. The spectrum also presents

a C=O stretching band at about 1750 cm^{-1} ($\nu_{C=O}$) due to residual ascorbic acid molecules adsorbed on the surface of the nanorods. The spectrum of the AuNR-Cu(I) conjugate is dominated by vibrations related to the ascorbic acid adsorbed on the AuNRs surface. Besides the peaks related to C-H stretching (ν_{C-H}) and bending (δ_{C-H}), which are found approximately in the same positions as the corresponding peaks in the spectrum of the Cu(I) complex, we observe an intense O-H stretching (ν_{O-H}) located at 3350 cm^{-1} and related to the many O-H groups of ascorbic acid. Two peaks related to C=O stretching bands are found at 1750 and 1680 cm^{-1}; the second one is due to the ester moiety of the ascorbic acid. Peaks related to the stretching of the C-O bonds of the ester and alcohol functions of ascorbic acid are found at 1280 and 1020 cm^{-1} respectively. The C-N stretching band of $[Cu(PTA)_4]BF_4$ (νC-N) and the band due to the BF_4^- anion (ν_{B-F}) are also visible in the spectrum as a consequence of the Cu(I) complex immobilization on the AuNR surface [56].

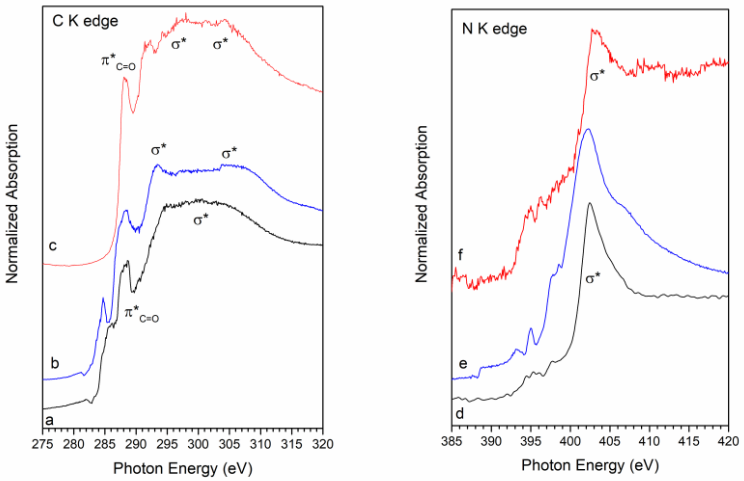

Figure 7. C K edge NEXAFS spectra of (a) AuNRs, (b) $[Cu(PTA)_4]BF_4$, (c) AuNR-Cu(I); N K edge NEXAFS spectra of (d) AuNRs, (e) $[Cu(PTA)_4]BF_4$, (f) AuNR-Cu(I).

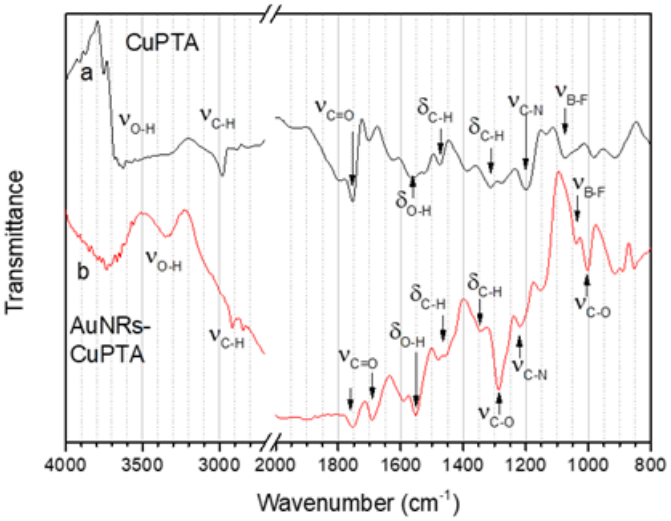

Figure 8. FTIR-spectra of (a) $[Cu(PTA)_4]BF_4$ and (b) AuNR-Cu(I) in the 4000–2700 cm^{-1} and 2000–800 cm^{-1} regions.

3.6. Biological Tests

To analyze the biocompatibility of AuNRs, the Vero E6 cell line was employed. This normal/immortalized cell line represents a useful model to perform viral propagation, vaccine production and biocompatibility assays. Vero E6 cells were treated with different concentrations of AuNRs (0.025, 0.05, 0.25, 0.5 and 1 μg/mL) for 24, 48, and 72 h,

and the measurement of cell viability was carried out by an MTT assay. The results are shown in Figure 9 and are in agreement with other studies performed with biocompatible AuNRs [57–60].

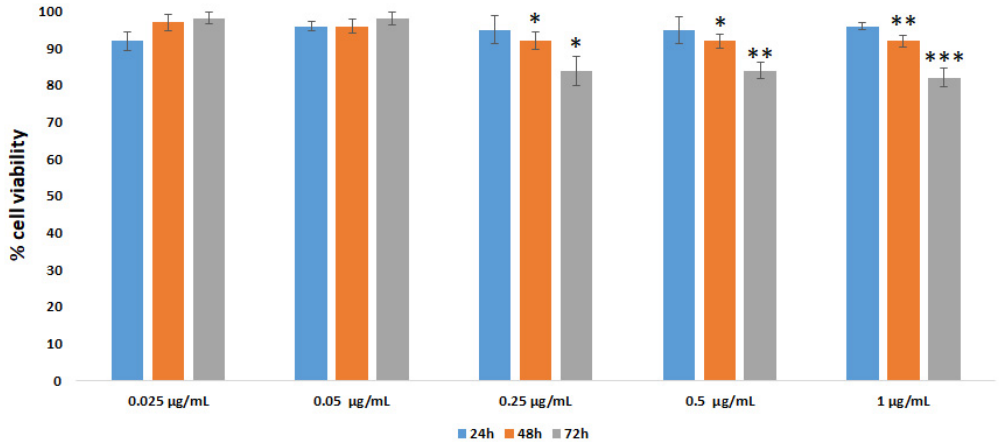

Figure 9. Vero E6 cell viability evaluated by the MTT test. Cells were incubated with AuNRs at different concentrations and treatment times. Data are expressed as % of cell viability with respect to the control (set at 100% value). All experiments were conducted in triplicate in at least three independent experiments. Results are expressed as mean ± SD values. * $p < 0.05$, ** $p < 0.01$, *** $p < 0.001$ (GraphPad Prism 10, unpaired *t*-test).

Next, Vero cells were incubated with the $[Cu(PTA)_4]BF_4$ coordination compound employed at concentrations between 1 and 50 µM for 24, 48 and 72 h to analyze the biocompatibility. It can be seen that this coordination compound induced a small reduction in cell viability (nearly 15–20%) after the 24 h treatment, which reached approximately 30% after the 48 and 72 h treatments (Figure 10). This behavior is consistent with analogous studies [61,62].

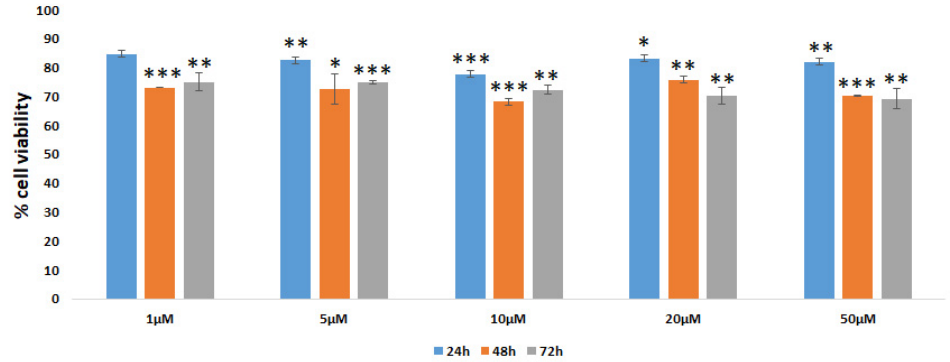

Figure 10. Vero E6 cell viability evaluated by MTT test. Cells were incubated with $[Cu(PTA)_4]BF_4$ at different concentrations and treatment times. Data are expressed as % of cell viability with respect to the control (set at 100% value). All experiments were conducted in triplicate in at least three independent experiments. Results are expressed as mean ± SD values. * $p < 0.05$, ** $p < 0.01$, *** $p < 0.001$ (GraphPad Prism 10, unpaired *t*-test).

Finally, the effect of treatment with different concentrations of AuNR-Cu(I) complex (obtained after conjugation of AuNRs with the $[Cu(PTA)_4]BF_4$ coordination compound) on Vero E6 cell viability was evaluated by an MTT assay for up to 72 h. As shown in Figure 11, a slight reduction in cell viability could be observed after treatments with 0.025 and 0.05 µg/mL for 24 h (a 20% reduction value as calculated with respect to a control sample set at 100%). Incubation for longer times or with higher AuNR-Cu(I) conjugate doses (0.25, 0.5 and 1 µg/mL) caused a minimal cell viability reduction (30 to 40%).

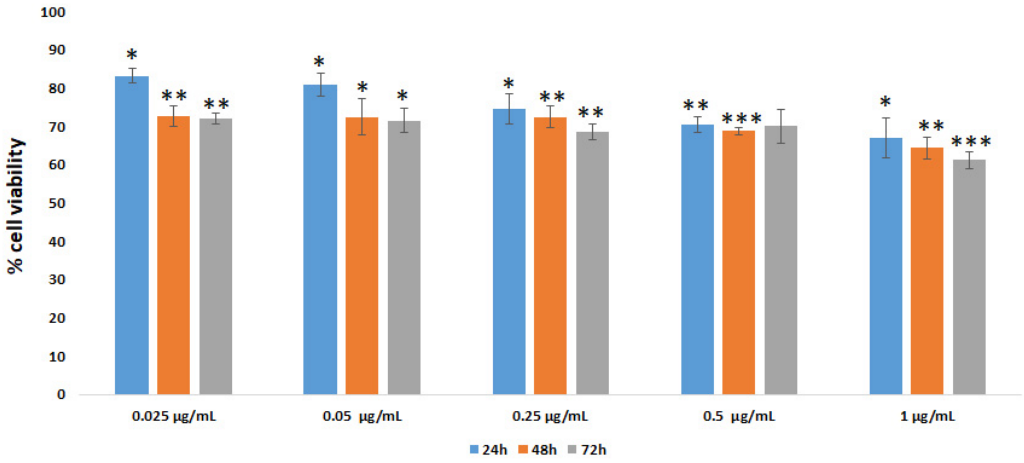

Figure 11. Vero E6 cell viability evaluated by MTT test. Cells were incubated with AuNR-Cu(I) at different concentrations and treatment times. Data are expressed as % of cell viability with respect to the control (set at 100% value). All experiments were conducted in triplicate in at least three independent experiments. Results are expressed as mean ± SD values. * $p < 0.05$, ** $p < 0.01$, *** $p < 0.001$ (GraphPad Prism 10, unpaired *t*-test).

The results obtained from the biological assessments indicated that the AuNRs, the Cu coordination compound $[Cu(PTA)_4]BF_4$, and the AuNR-Cu(I) conjugate induced no or a very light reduction in Vero E6 cell viability, strongly suggesting good biocompatibility. These results are a promising example of the use of our selected copper complexes conjugated with AuNRs as versatile biocompatible anisotropic chemical drug delivery systems. In fact, this conjugate system will apply to applications in antiviral treatment strategies, using Vero cells as a reference normal culture or cell-culture-based infection model for viral replication [63].

4. Conclusions

In this work, the synthesis of highly hydrophilic gold nanorods was studied and implemented, exploiting the two-step wet method. The objective of obtaining a system for the transport of copper(I)-based drugs was thus achieved. TEM observations showed AuNRs with regular shapes and sizes, with an AR of 2.6, confirmed by DLS and ζ potential measurements. The AuNRs were conjugated with a Cu(I)-based drug, i.e., $[Cu(PTA)_4]BF_4$ (PTA = 1,3,5- triaza-7-phosphadamantane), obtaining a loading efficiency of η (%) = 50 ± 10%. The conjugate system was characterized using different spectroscopies (UV–Vis–NIR, FT-IR, and XPS), which verified the surface functionalization and Cu(I)-Au interaction. To study the biocompatibility of conjugated and non-conjugated AuNRs, MTT assays were performed with Vero E6 cells. These experiments showed a reduction in biocompatibility only for high concentrations (1 µg/mL) and long times (72 h), confirming the high applicative potential of the conjugated system in nanomedicine and, in particular, for innovative antiviral treatment strategies.

Supplementary Materials: The following supporting information can be downloaded at https://www.mdpi.com/article/10.3390/nano16030217/s1: Table S1: Experimental details of gold nanorod synthesis. Table S2: Experimental details of drug conjugation. Figure S1: (a) ζ potential measurements of AuNRs performed immediately after synthesis (blue line, ζ potential = 46 ± 4 mV) and after 3 months (orange line, ζ potential = 53 ± 6 mV); (b) ζ potential measurements of AuNR-Cu(I) performed after 9 months from conjugation, ζ potential = −27 ± 7 mV. Table S3: XPS data (BE, FWHM, atomic ratio values and proposed assignments) collected from AuNRs, AuNR-Cu(I) and Cu(I) complex.

Author Contributions: E.O., S.A. and I.V.: AuNR synthesis and Cu(I) complexes loading studies; E.O., A.S., M.C. (Marisa Colone), A.C. and M.L.D.: TEM, biological investigations, and their data curations; G.I., L.T. and E.M.: FTIR and NIR investigations and their data curations; D.L., M.M., S.A. and C.B.: synchrotron investigations and data curations and resources; M.C. (Miriam Caviglia), J.D.G., C.S. and M.P.: synthesis of Cu(I) complexes; G.A., A.P. and F.T.: UV–Vis–NIR studies on conjugated systems; V.-A.M. for TEM images; I.V.: conceptualization, data curation, writing—original draft, supervision, writing—review and editing. The manuscript was written through the contributions of all authors. All authors have read and agreed to the published version of the manuscript.

Funding: This research was partially funded by the Grant of Excellence Departments 2023–2027, MIUR (ARTICOLO 1, COMMI 314–337 LEGGE 232/2016), in particular with the purchase of the Zetasizer Ultra Red instrument from Malvern, and Rome Technopole Project CUP: F83B22000040006. This research was partially funded by Istituto Superiore di Sanità, ISS (Ministry of Health—ISS funding, ISS funding, FARV 24-25). This work was supported by Unione Europea—NextGenerationEU (MUR-Fondo Promozione e Sviluppo—D.M. 737/2021, INVIRCuM, University of Camerino, FAR 2022 PNR, and NGEU PNRR, D.M. n. 351/2022 M4C1 I4.1).

Data Availability Statement: The original contributions presented in this study are included in the article/Supplementary Materials. Further inquiries can be directed to the corresponding author.

Acknowledgments: I.V., G.I., C.B., A.P., G.A. and F.T. recognize the support of the Framework Agreement signed between the CNR and the Sciences Department of the University of Roma Tre. The authors from Roma Tre gratefully acknowledge the CERIC-ERIC Consortium for the access to experimental facilities (SuperESCA at Elettra, LISA at ESRF, HR-TEM@NIMP) and financial support (experiment #20232011), and the synchrotron radiation implant Elettra for access to experimental facilities (BEAR, experiment #20230160) and partial financial support. VAM acknowledges the financial support from the Romanian Ministry of Research, Innovation and Digitalization through the Core Program of the National Institute of Materials Physics under Project PC1-PN23080101.

Conflicts of Interest: The authors declare no competing financial interests.

References

1. Xia, K.; Yatabe, T.; Yonesato, K.; Kikkawa, S.; Yamazoe, S.; Nakata, A.; Ishikawa, R.; Shibata, N.; Ikuhara, Y.; Yamaguchi, K.; et al. Ultra-stable and highly reactive colloidal gold nanoparticle catalysts protected using multi-dentate metal oxide nanoclusters. *Nat. Commun.* **2024**, *15*, 851. [CrossRef] [PubMed]
2. Dehkordi, S.M.; Mohammadi, H. Improvement of directivity in plasmonic nanoantennas based on structured cubic gold nanoparticles. *Sci. Rep.* **2024**, *14*, 17153. [CrossRef] [PubMed]
3. Naponiello, G.; Venditti, I.; Zardetto, V.; Saccone, D.; Di Carlo, A.; Fratoddi, I.; Barolo, C.; Dini, D. Photoelectrochemical characterization of squaraine-sensitized nickel oxide cathodes deposited via screen-printing for p-type dye-sensitized solar cells. *Appl. Surf. Sci.* **2015**, *356*, 911–920. [CrossRef]
4. Junior, B.B.; Sawazaki, M.R.B.; Guidelli, É.J.; Mulato, M. Optimizing gold nanoparticles for thin film formation: Insights into synthesis and surface functionalization with APTES. *Colloids Surf. A Physicochem. Eng. Asp.* **2025**, *722*, 137–180. [CrossRef]
5. Zarska, M.; Novak, O.; Jakubcova, T.; Novotny, F.; Urbancokova, A.; Havel, F.; Novak, J.; Raabova, H.; Musilek, K.; Filimonenko, V.; et al. Photothermal induction of pyroptosis in malignant glioma spheroids using (16-mercaptohexadecyl) trimethyl ammonium bromide-modified cationic gold nano-rods. *Colloids Surf. B Biointerfaces* **2024**, *243*, 114128. [CrossRef]
6. Elsayed, D.A.; Assy, M.G.; Mousa, S.M.; El-Bassyouni, G.T.; Mouneir, S.M.; Shehab, W.S. TiO_2 nanoparticle as catalyst for an efficient green one-pot synthesis of 1H-3-Indolyl Derivatives as significant antiviral activity. *Bioorg. Chem.* **2022**, *124*, 105805. [CrossRef]
7. Venditti, I.; Barbero, N.; Russo, M.V.; Di Carlo, A.; Decker, F.; Fratoddi, I.; Barolo, C.; Dini, D. Electrodeposited ZnO with squaraine sentisizers as photoactive anode of DSCs. *Mater. Res. Express* **2014**, *1*, 015040. [CrossRef]
8. Zhou, W.; Yao, Y.; Qin, H.; Xing, X.; Li, Z.; Ouyang, M.; Fan, H. Size Dependence of Gold Nanorods for Efficient and Rapid Photothermal Therapy. *Int. J. Mol. Sci.* **2024**, *25*, 2018. [CrossRef]
9. Kim, N.; Jeong, Y.-G.; Lee, S.; Kang, J.; Kim, Y.; Choi, Y.-A.; Khang, D.; Kim, S.-H. Ameliorated Skin Inflammation through the Synergistic Effect of Gold Nano-rod–Dexamethasone and Photothermal Therapy. *ACS Appl. Mater. Interfaces* **2024**, *16*, 12217–12231. [CrossRef]

10. Sílvia, S.; Aires, F.; Monteiro, A.; Pinto, G.; Faria, I.; Sales, G.; Correa-Duarte, M.A.; Guerreiro, S.; Fernandes, R. Radiotherapy Metastatic Prostate Cancer Cell Lines Treated with Gold Nano-rods Modulate miRNA Signatures. *Int. J. Mol. Sci.* **2024**, *25*, 2754. [CrossRef]
11. Chakraborty, K.; Biswas, A.; Mishra, S.; Mallick, A.M.; Tripathi, A.; Jan, S.; Roy, R.S. Harnessing Peptide-Functionalized Multivalent Gold Nanorods for Promoting Enhanced Gene Silencing and Managing Breast Cancer Metastasis. *ACS Appl. Bio Mater.* **2023**, *6*, 458–472. [CrossRef] [PubMed]
12. Arsalani, S.; Arsalani, S.; Isikawa, M.; Guidelli, E.J.; Mazon, E.E.; Ramos, A.P.; Bakuzis, A.; Pavan, T.Z.; Baffa, O.; Carneiro, A.A.O. Hybrid Nanoparticles of Citrate-Coated Manganese Ferrite and Gold Nanorods in Magneto-Optical Imaging and Thermal Therapy. *Nanomaterials* **2023**, *13*, 434. [CrossRef] [PubMed]
13. Khan, A.; Khan, T.H.; Ahamed, M.; El-Toni, A.M.; Aldalbahi, A.; Alam, J.; Ahamad, T. Temperature-Responsive Polymer Microgel-Gold Nanorods Composite Particles: Physicochemical Characterization and Cytocompatibility. *Polymers* **2018**, *10*, 99. [CrossRef] [PubMed]
14. Pissuwan, D.; Poomrattanangoon, S.; Chungchaiyart, P. Trends in Using Gold Nanoparticles for Inducing Cell Differentiation: A Review. *ACS Appl. Nano Mater.* **2022**, *5*, 3110–3120. [CrossRef]
15. Kruse, B.; Dash, B.S.; Kostka, K.; Wolff, N.; Prymak, O.; Loza, K.; Gumbiowski, N.; Heggen, M.; Oliveira, C.L.P.; Chen, J.-P.; et al. Doxorubicin-Loaded Ultrasmall Gold Nanoparticles (1.5 nm) for Brain Tumor Therapy and Assessment of Their Biodistribution. *ACS Appl. Bio Mater.* **2024**, *7*, 6890–6907. [CrossRef]
16. Wang, S.; Zhao, X.; Wang, S.; Qian, J.; He, S. Biologically Inspired Polydopamine Capped Gold Nanorods for Drug Delivery and Light-Mediated Cancer Therapy. *ACS Appl. Mater. Interfaces* **2016**, *8*, 24368–24384. [CrossRef]
17. Zygouri, E.; Bekiari, V.; Malis, G.; Karamanos, N.K.; Koutsakis, C.; Psomas, G.; Tangoulis, V. pH-Sensitive Gold Nanorods for Non-Steroidal Anti-Inflammatory Drugs (NSAIDs) Delivery and DNA-Binding Studies. *Molecules* **2023**, *28*, 3780. [CrossRef]
18. He, J.; He, Y.; Wu, X.; Zhang, X.; Hu, R.; Tang, B.Z.; Xu, Q.-H. Mesoporous Silica-Encapsulated Gold Nanorods for Drug Delivery/Release and Two-Photon Excitation Fluorescence Imaging to Guide Synergistic Phototherapy and Chemotherapy. *ACS Appl. Bio Mater.* **2023**, *6*, 3433–3440. [CrossRef]
19. Linnell, B.M.P.; Noveron, J.C. Gold nanoparticles with reversible colloidal aggregation mediated with Cu (II) ions. *Colloids Surf. A Physicochem. Eng. Asp.* **2023**, *682*, 132806. [CrossRef]
20. Zhou, R.; Zhang, M.; Xi, J.; Li, J.; Ma, R.; Ren, L.; Bai, Z.; Qi, K.; Li, X. Gold Nano-rods-Based Photothermal Therapy: Interactions Between Biostructure, Nanomaterial, and Near-Infrared Irradiation. *Nanoscale Res. Lett.* **2022**, *17*, 68. [CrossRef]
21. Chen, Y.-S.; Zhao, Y.; Yoon, S.J.; Gambhir, S.S.; Emelianov, S. Miniature gold nanorods for photoa-coustic molecular imaging in the second near-infrared optical window. *Nat. Nanotechnol.* **2019**, *14*, 465–472. [CrossRef] [PubMed]
22. Zhao, S.; Luo, Y.; Chang, Z.; Liu, C.; Li, T.; Gan, L.; Huang, Y.; Sun, Q. BSA-Coated Gold Nanorods for NIR-II Photothermal Therapy. *Nanoscale Res. Lett.* **2021**, *16*, 170. [CrossRef] [PubMed]
23. Wang, Y.; Wu, Y.; Wen, Q.; Li, P.; Wang, Y.; Jiang, H.; Zhang, W. PEGylated gold nano-rods with a broad absorption band in the first near-infrared window for in vivo multifunctional photoa-coustic imaging. *RSC Adv.* **2020**, *10*, 4561–4567. [CrossRef] [PubMed]
24. Wen, X.; Bi, S.; Zeng, S. NIR-II Light-Activated Gold Nanorods for Synergistic Thermo-dynamic and Photothermal Therapy of Tumor. *ACS Appl. Bio Mater.* **2023**, *6*, 1934–1942. [CrossRef]
25. Ngece, K.; Khwaza, V.; Paca, A.M.; Aderibigbe, B.A. The Antimicrobial Efficacy of Copper Complexes: A Review. *Antibiotics* **2025**, *14*, 516. [CrossRef]
26. Guz-Regner, K.; Komarnicka, U.K.; Futoma-Kołoch, B.; Wernecki, M.; Cal, M.; Kozieł, S.; Ziółkowska, A.; Bugla-Płoskońska, G. Antibacterial activity and action mode of Cu(I) and Cu(II) complexes with phosphines derived from fluoroquinolone against clinical and multidrug-resistant bacterial strains. *J. Inorg. Biochem.* **2020**, *210*, 111124. [CrossRef]
27. Ammerman, N.C.; Beier-Sexton, M.; Azad, A.F. Growth and maintenance of Vero cell lines. *Curr. Protoc. Microbiol.* **2008**, *11*, A.4E.1–A.4E.7. [CrossRef]
28. Ayon, N.J. High-Throughput Screening of Natural Product and Synthetic Molecule Libraries for Antibacterial Drug Discovery. *Metabolites* **2023**, *13*, 625. [CrossRef]
29. Parra, B.; Contreras, A.; Mina, J.H.; Valencia, M.E.; Grande-Tovar, C.D.; Valencia, C.H.; Ramírez, C.; Bolívar, G.A. The Entrapment and Concentration of SARS-CoV-2 Particles with Graphene Oxide: An In Vitro Assay. *Nanomaterials* **2023**, *13*, 343. [CrossRef]
30. Zhu, Y.; Binder, J.; Yurgelonis, I.; Rai, D.K.; Lazarro, S.; Costales, C.; Kobylarz, K.; McMonagle, P.; Steppan, C.M.; Aschenbrenner, L.; et al. Generation of a VeroE6 Pgp gene knock out cell line and its use in SARS-CoV-2 antiviral study. *Antivir. Res.* **2022**, *208*, 105429. [CrossRef]
31. Yamate, M.; Yamashita, M.; Goto, T.; Tsuji, S.; Li, Y.-G.; Warachit, J.; Yunoki, M.; Ikuta, K. Establishment of Vero E6 cell clones persistently infected with severe acute respiratory syndrome coronavirus. *Microbes Infect.* **2005**, *7*, 1530–1540. [CrossRef] [PubMed]

32. Santini, C.; Pellei, M.; Papini, G.; Morresi, B.; Galassi, R.; Ricci, S.; Tisato, F.; Porchia, M.; Rigobello, M.P.; Gandin, V.; et al. In vitro antitumour activity of water soluble Cu(I), Ag(I) and Au(I) complexes supported by hydrophilic alkyl phosphine ligands. *J. Inorg. Biochem.* **2011**, *105*, 232–240. [CrossRef] [PubMed]
33. Lopez, A.; Amatori, S.; Olivieri, E.; Venditti, I.; Iucci, G.; Meneghini, C.; Bertelà, F.; Del Bello, F.; Quaglia, W.; Pellei, M.; et al. Cu (I) Coordination Compounds Conjugated to Au Nanorods for Future Applications in Drug Delivery: Insights in Molecular, Electronic and Cu Local Structure in Solid and Liquid Phase. *ChemPhysChem* **2024**, *25*, e202400074. [CrossRef] [PubMed]
34. Amatori, S.; Lopez, A.; Meneghini, C.; Calcabrini, A.; Colone, M.; Stringaro, A.; Migani, S.; Khalakhan, I.; Iucci, G.; Venditti, I.; et al. Gold nanorods derivatized with CTAB and hydroquinone or ascorbic acid: Spectroscopic investigation of anisotropic nanoparticles of different shapes and sizes. *Nanoscale Adv.* **2023**, *5*, 3924–3933. [CrossRef]
35. Nikoobakht, B.; El-Sayed, M.A. Preparation and Growth Mechanism of Gold Nanorods (NRs) Using Seed-Mediated Growth Method. *Chem. Mater.* **2003**, *15*, 1957–1962. [CrossRef]
36. Gandin, V.; Tisato, F.; Dolmella, A.; Pellei, M.; Santini, C.; Giorgetti, M.; Marzano, C.; Porchia, M. In Vitro and in Vivo Anticancer Activity of Copper(I) Complexes with Homoscorpionate Tridentate Tris(pyrazolyl)borate and Auxiliary Monodentate Phosphine Ligands. *J. Med. Chem.* **2014**, *57*, 4745–4760. [CrossRef]
37. Fratoddi, I.; Venditti, I.; Battocchio, C.; Carlini, L.; Amatori, S.; Porchia, M.; Tisato, F.; Bondino, F.; Magnano, E.; Pellei, M.; et al. Highly hydrophilic gold nanoparticles as carrier for anticancer copper(I) complexes: Loading and release studies for biomedical applications. *Nanomaterials* **2019**, *9*, 772. [CrossRef]
38. Venditti, I.; Cartoni, A.; Cerra, S.; Fioravanti, R.; Salamone, T.A.; Sciubba, F.; Tabocchini, M.A.; Dini, V.; Battocchio, C.; Iucci, G.; et al. Hydrophilic Gold Nanoparticles as anti-PD-L1 Antibody carriers: Synthesis and Interface Properties. *Part. Part. Syst. Charact.* **2022**, *39*, 4. [CrossRef]
39. Liu, H.; Pierre-Pierre, N.; Huo, Q. Dynamic light scattering for gold nanorod size characterization and study of nanorod–protein interactions. *Gold Bull.* **2012**, *45*, 187–195. [CrossRef]
40. Cametti, C.; Fratoddi, I.; Venditti, I.; Russo, M.V. Dielectric relaxations of thiol-coated noble metal nano-particles in aqueous solutions: Electrical characterization of the interface. *Langmuir* **2011**, *27*, 7084–7090. [CrossRef]
41. Zhu, J.; Huang, L.; Zhao, J.; Wang, Y.; Zhao, Y.; Hao, L.; Lu, Y. Shape dependent resonance light scattering properties of gold nanorods. *Mater. Sci. Eng. B* **2005**, *121*, 199–203. [CrossRef]
42. Venditti, I.; Fratoddi, I.; Palazzesi, C.; Prosposito, P.; Casalboni, M.; Cametti, C.; Battocchio, C.; Polzonetti, G.; Russo, M.V. Self-assembled nanoparticles of functional copolymers for photonic applications. *J. Colloids Interface Sci.* **2010**, *348*, 424–430. [CrossRef] [PubMed]
43. Nikolopoulou, S.G.; Kalska, B.; Basa, A.; Papadopoulou, A.; Efthimiadou, E.K. Novel Hybrid Silver−Silica Nanoparticles Synthesized by Modifications of the Sol−Gel Method and Their Theranostic Potential in Cancer. *ACS Appl. Bio Mater.* **2023**, *6*, 5235−5251. [CrossRef] [PubMed]
44. NIST. *X-Ray Photoelectron Spectroscopy Database, NIST Standard Reference Database Number 20*; National Institute of Standards and Technology: Gaithersburg, MD, USA, 2000; p. 20899. Available online: https://doi.org/10.18434/T4T88K (accessed on 24 November 2023).
45. Huang, S.-H.; Peng, S.; Wang, Q.-Y.; Hu, Q.-H.; Zhang, R.-Q.; Liu, L.; Liu, Q.; Lin, J.; Zhou, Q.-H. Gold nanorods con-jugated with biocompatible zwitterionic polypeptide for combined chemo-photothermal therapy of cervical cancer. *Colloids Surf. B Biointerfaces* **2021**, *207*, 112014. [CrossRef]
46. Venditti, I.; Iucci, G.; Fratoddi, I.; Cipolletti, M.; Montalesi, E.; Marino, M.; Secchi, V.; Battocchio, C. Directly Resveratrol immobilization on hydrophilic charged gold nanoparticles: Structural investigations and cytotoxic studies for Biomedical Applications. *Nanomaterials* **2020**, *10*, 1898. [CrossRef]
47. Zhi, X.; Jiang, Y.; Xie, L.; Li, Y.; Fang, C.-J. Gold Nanorods Functionalized with Cathepsin B Targeting Peptide and Doxorubicin for Combinatorial Therapy against Multidrug Resistance. *ACS Appl. Bio Mater.* **2019**, *2*, 5697–5706. [CrossRef]
48. Sun, J.; Li, L.; Cai, W.; Chen, A.; Zhang, R. Multifunctional Hybrid Nanoprobe for Photoacoustic/PET/MR Imaging-Guided Photothermal Therapy of Laryngeal Cancer. *ACS Appl. Bio Mater.* **2021**, *4*, 5312–5323. [CrossRef]
49. Xiao, Y.; Hong, H.; Matson, V.Z.; Javadi, A.; Xu, W.; Yang, Y.; Zhang, Y.; Engle, J.W.; Nickles, R.J.; Cai, W.; et al. Gold Nanorods Conjugated with Doxorubicin and cRGD for Combined Anticancer Drug Delivery and PET Imaging. *Theranostics* **2012**, *2*, 757–768. [CrossRef]
50. Awan, U.A.; Raza, A.; Ali, S.; Saeed, R.F.; Akhtar, N.; Beilstein, J. Doxorubicin-loaded gold nanorods: A multifunctional chemo-photothermal nanoplatform for cancer management. *Beilstein J. Nanotechnol.* **2021**, *12*, 295–303. [CrossRef]
51. Liu, M.; Guyot-Sionnest, P. Mechanism of Silver(I)-Assisted Growth of Gold Nanorods and Bipyramids. *J. Phys. Chem. B* **2005**, *109*, 22192–22200. [CrossRef]
52. Grzelczak, M.; Pérez-Juste, J.; Rodríguez-González, B.; Liz-Marzán, L.M. Influence of silver ions on the growth mode of platinum on gold nanorods. *J. Mater. Chem.* **2006**, *16*, 3946–3951. [CrossRef]

53. Beamson, G.; Briggs, D. *High Resolution XPS of Organic Polymers: The Scienta ESCA 300 Database*; John Wiley & Sons: Chichester, UK, 1992.
54. Ward, C.J.; Tronndorf, R.; Eustes, A.S.; Auad, M.L.; Davis, E.W. Seed-Mediated Growth of Gold Nano-rods: Limits of Length to Diameter Ratio Control. *J. Nanomater.* **2014**, *2014*, 765618. [CrossRef]
55. Burrows, N.D.; Harvey, S.; Idesis, F.A.; Murphy, C.J. Understanding the Seed-Mediated Growth of Gold Nanorods through a Fractional Factorial Design of Experiments. *Langmuir* **2017**, *33*, 1891–1907. [CrossRef] [PubMed]
56. Secchi, V.; Franchi, S.; Ciccarelli, D.; Dettin, M.; Zamuner, A.; Serio, A.; Iucci, G.; Battocchio, C. Biofunctionalization of TiO_2 Surfaces with Self-Assembling Layers of Oligopeptides Covalently Grafted to Chitosan. *ACS Biomater. Sci. Eng.* **2019**, *5*, 2190−2199. [CrossRef]
57. Fernando, D.; Sulthana, S.; Vasquez, Y. Cellular Uptake and Cytotoxicity of Varying Aspect Ratios of Gold Nanorods in HeLa Cells. *ACS Appl. Bio Mater.* **2020**, *3*, 1374−1384. [CrossRef]
58. Binelli, L.; Dini, V.; Amatori, S.; Scotognella, T.; Giordano, A.; De Berardis, B.; Bertelà, F.; Battocchio, C.; Iucci, G.; Fratoddi, I.; et al. Gold nanorods as vehicle for radiopharmaceuticals: Preparation and preliminary radiobiological in vitro tests. *Nanomaterials* **2023**, *13*, 1898. [CrossRef]
59. Alkilany, A.M.; Nagaria, P.K.; Hexel, C.R.; Shaw, T.J.; Murphy, C.J.; Wyatt, M.D. Cellular uptake and cytotoxicity of gold nanorods: Molecular origin of cytotoxicity and surface effects. *Small* **2009**, *5*, 701−708. [CrossRef]
60. Hu, M.; Wen, C.; Liu, J.; Cai, P.; Meng, N.; Qin, X.; Xu, P.; Li, Z.; Lin, X.-C. Mechanism of Cytotoxic Action of Gold Nanorods Photothermal Therapy for A549 Cell. *ACS Appl. Bio Mater.* **2023**, *6*, 1886–1895. [CrossRef]
61. Artiga, Á.; García-Embid, S.; De Matteis, L.; Mitchell, S.G.; de la Fuente, J.M. Effective in Vitro Photokilling by Cell-Adhesive Gold Nanorods. *Front. Chem.* **2018**, *6*, 234. [CrossRef]
62. Elste, J.; Kumari, S.; Sharma, N.; Razo, E.P.; Azhar, E.; Gao, F.; Nunez, M.C.; Anwar, W.; Mitchell, J.C.; Tiwari, V.; et al. Plant Cell-Engineered Gold Nanoparticles Conjugated to Quercetin Inhibit SARS-CoV-2 and HSV-1 Entry. *Int. J. Mol. Sci.* **2023**, *24*, 14792. [CrossRef]
63. Tavakoli, A.; Hashemzadeh, M.S. Inhibition of herpes simplex virus type 1 by copper oxide nanoparticles. *J. Virol. Methods* **2020**, *275*, 113688. [CrossRef]